ACS MEASUREMENT SCIENCE Au
AN OPEN ACCESS JOURNAL OF THE AMERICAN CHEMICAL SOCIETY

pubs.acs.org/measureau
Article

Comparison of Different Vibrational Spectroscopic Probes (ATR-FTIR, O-PTIR, Micro-Raman, and AFM-IR) of Lipids and Other Compounds Found in Environmental Samples: Case Study of Substrate-Deposited Sea Spray Aerosols

Carolina Molina, Deborah Kim, Lincoln Mehndiratta, Jennie Lee, Chamika K. Madawala, Jonathan H. Slade, Alexei V. Tivanski, and Vicki H. Grassian*

Cite This: https://doi.org/10.1021/acsmeasuresciau.4c00033
Read Online

ABSTRACT: The use of vibrational spectroscopy to probe environmental samples is increasing with the development of new methods, including microspectroscopic probes. In this study, we compare different vibrational methods to interrogate lipids and other compounds found in environmental samples. In particular, we compare the vibrational spectra for different lipids that include fatty acids (protonated and deprotonated forms), fatty alcohols, and fatty esters by utilizing attenuated total reflection Fourier transform infrared (ATR-FTIR) spectroscopy, optical photothermal infrared (O-PTIR) spectroscopy, micro-Raman spectroscopy, and atomic force microscopy infrared (AFM-IR) spectroscopy. We show the utility of infrared methods to clearly delineate the structure of the lipid, i.e., whether it is an acid, alcohol, or ester. In contrast, it is difficult to differentiate these from micro-Raman spectroscopy. Furthermore, in the case of fatty acids, the protonation state can also be determined by infrared methods. In most cases, there is a high correlation between the three different infrared techniques as seen for ATR-FTIR and O-PTIR spectroscopy; however, this is not always true with AFM-IR spectroscopy for samples with low signal-to-noise or in a liquid phase state. Additionally, substrate-deposited aerosols were collected from the Scripps Ocean-Atmosphere Research Simulator (SOARS) and examined with both the O-PTIR and micro-Raman spectroscopy to show how these two vibrational probes together can provide essential chemical insights into environmental samples that are difficult to achieve otherwise.

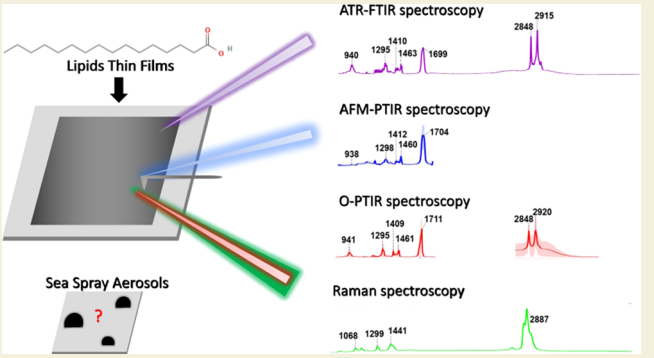

KEYWORDS: *aerosols, lipids, environmental samples, microspectroscopy, hyperspectral mapping, vibrational spectroscopy*

INTRODUCTION

Resolving the chemical composition of complex mixtures in environmental samples is challenging due to many factors, such as sample collection, sample preparation, sample destruction, and length of time for analysis.[1−4] Spectroscopy combined with various imaging techniques has emerged as a valuable tool to overcome some of these challenges. It has been used due to its sensitivity and imaging capabilities, allowing for the visualization of the chemical distribution within different types of samples.[1,5,6] In addition, many of these techniques do not require extensive sample preparation and are nondestructive.[7]

Aerosols are widely studied due to their impacts on atmospheric chemistry, climate, and human health.[8−10] Online and offline spectroscopic techniques have been broadly employed to measure the composition and properties of aerosols. While online techniques provide in situ data without the need for sample collection and storage, they may be limited when a more detailed physicochemical analysis is required.[11] Analyzing substrate-deposited ambient aerosols, such as sea spray aerosols (SSA), presents several difficulties due to their broad size distribution and different mixing states of diverse chemicals. For substrate-deposited aerosols, various techniques are utilized including atomic force microscopy, scanning electron microscopy, and transmission electron microscopy. These techniques are often coupled with other methods of analysis including energy-dispersed X-rays, energy loss spectroscopy, near-edge X-ray absorption fine structure spectros-

Received: July 1, 2024
Revised: October 22, 2024
Accepted: October 23, 2024

copy, proton-induced X-ray emission, fluorescence microscopy, micro-Raman spectroscopy, and micro-Fourier transform infrared (FTIR) spectrosocpy.[12−16]

Vibrational spectroscopy, in particular, can provide valuable information related to molecular speciation, water content, and phase state.[14] Micro-Raman and infrared (IR) spectroscopy are complementary techniques, as vibrational modes active in Raman spectroscopy may not be active in IR spectroscopy and vice versa.[16] The use of vibrational microspectroscopic probes of environmental samples has expanded in the past decade. Micro-Raman spectroscopy has been particularly useful in determining SSA's chemical composition and heterogeneous reactivity, although sample fluorescence can be a limiting factor.[11,17−24] Micro-Raman spectroscopy has a better spatial resolution than micro-FTIR spectroscopy. However, in recent years, the development of photothermal infrared spectroscopy has introduced new methods for the infrared analysis of individual particles at high spatial resolution. In particular, AFM coupled with photothermal IR (AFM-IR) spectroscopy and optical photothermal IR (O-PTIR) spectroscopy has been utilized as nanoscale and microscale probes, respectively, for a wide range of particles from sub-100 nm to above 10 μm or larger in dimension.

AFM-IR spectroscopy is a powerful high-resolution imaging technique that provides information about individual particles' surface morphology, phase, and topography. It operates by detecting the mechanical response of the samples induced by photothermal effects through the deflection of the AFM cantilever tip. Valuable information from the infrared spectrum of the sample can be extracted from point spectra and spectral maps.[25−27] Like micro-Raman spectroscopy, AFM-IR spectroscopy allows for controlling environmental conditions, including relative humidity and temperature, by using an environmental cell. Both techniques have been utilized to investigate ice nucleation and hygroscopicity of SSA.[17,28] O-PTIR spectroscopy combines the sensitivity of IR spectroscopy with high spatial resolution on the order of 0.5 μm.[29] Unlike AFM-IR spectroscopy, O-PTIR spectroscopy does not involve a mechanical probe. This allows for analyzing and mapping a wider variety of heterogeneous samples with high surface roughness or are more liquid-like, which are current limitations of AFM-IR spectroscopy. In the case of O-PTIR spectroscopy, an IR laser is used for local heating, while a visible laser (probe laser) collects the scattered light and measures changes in the refractive index due to heating from the absorption of infrared light at resonant frequencies. This instrument can be coupled with a monochromator and a CCD detector enabling the simultaneous collection of micro-Raman spectra.[30−34]

Despite significant advancements in vibrational technologies, identifying compounds in highly complex samples remains a major challenge. Different approaches have been proposed to address this challenge. One approach has been using spectral libraries and databases of compounds to search for similar patterns (often employed with chemometrics tools like principal component analysis) and performing library matching that relies on spectral similarities.[35] However, one of the main difficulties is that many compounds have not been previously measured making them absent from spectral databases. Sample preparation, matrix effects, instrument variability, and spectral processing can additionally make compound identification difficult.[35,36] Moreover, most infrared spectral databases are based on FTIR spectroscopy; however, for complex environmental samples, especially for aerosol particles deposited on substrates, other vibrational techniques with higher spatial resolution can be more suitable to interrogate individual deposited aerosol particles so as to better identify different populations within specific aerosol types including sea spray aerosols. Furthermore, light scattering, water uptake, heterogeneous reactivity, and cloud activation all occur at the single particle level and depend very specifically on the chemical composition and size of the aerosol particle. For single particle analysis, it is important to utilize microspectroscopic probes and preferably techniques that do not require a background spectrum as is typically needed in any absorption method. Therefore, vibrational techniques such as O-PTIR and AFM-IR spectroscopy are useful methods to interrogate individual, substrate-deposited aerosol particles. However, it is important to compare these methods to more traditional methods of infrared spectroscopy to determine similarities and differences.

To address some of these issues in a systematic way, we first compare several vibrational techniques for analyzing thin films of different lipids. Lipids are released by phytoplankton metabolic processes and cell lysis and are significant components of SSAs.[37−40] Due to their hydrophobic character, these molecules typically accumulate at the sea surface microlayer.[19,41,42] Thus, their presence is significant, as they can influence surface activity, water−air exchange flux, and SSA formation. Due to their stability and low degradation rates, they also serve as tracers for SSA and living organisms.[37] Specifically, we compare attenuated total reflection-Fourier transform infrared (ATR-FTIR), Optical Photothermal Infrared (O-PTIR), micro-Raman, and Atomic Force Microscopy-Infrared (AFM-IR) spectroscopy. Each technique operates based on different principles and, in some cases, different selection rules. We show that the infrared methods can easily differentiate between the different lipids and the fatty acids and their protonation states, whereas micro-Raman spectroscopy showed a limited ability to differentiate. Additionally, we utilized O-PTIR and micro-Raman spectroscopy to analyze the SSA generated from the Scripps Ocean-Atmosphere Research Simulator (SOARS). The analysis revealed the presence of diverse organic and inorganic compounds in SSA and demonstrated that O-PTIR spectroscopy is a powerful technique for characterizing complex SSA mixtures. Furthermore, by combining O-PTIR and micro-Raman spectroscopy, we show how these techniques provide insights into the different components that make up SSA and their distribution within individual particles.

MATERIALS AND METHODS

Reagents and Stock Solutions

For a comparison of different lipids, the following compounds were measured: palmitic acid, stearic acid, nonanoic acid, oleic acid, sodium palmitate, sodium nonanoate, sodium oleate, palmityl alcohol, and methyl palmitate. For most samples, stock solutions of these compounds were prepared at a concentration of 0.1 M in either Milli-Q water, ethanol, methanol, or chloroform, based on the compound solubility. Information regarding the providers of the compounds, preparation methods, and other compounds considered in this study is included in the Supporting Information (SI) Table S1.

Sample Preparation

Thin films of these different lipids were analyzed using the following different spectroscopic methods: ATR-FTIR, AFM-IR, O-PTIR, and micro-Raman. The thickness of the films ranged between 0.3 and 1 μm. To prepare the thin films, an aliquot of the stock solutions was deposited onto precleaned substrates which were allowed to air-dry

https://doi.org/10.1021/acsmeasuresciau.4c00033
ACS Meas. Sci. Au XXXX, XXX, XXX−XXX

completely for a minimum of 5 h. The substrates were selected for each technique for a minimum spectral interference and maximum signal-to-noise ratio. For ATR-FTIR, 1 mL of each solution was deposited onto an Amorphous Material Transmitting Infrared (AMTIR) crystal (Pike Technologies). In the case of AFM-IR and O-PTIR coupled with micro-Raman spectroscopy, 5 μL of solution was drop-cast onto a silica wafer (Ted Pella Inc.) and a calcium fluoride (CaF_2) substrate (Crystan Ltd.), respectively.

SSA Sample Collection

SSA samples were collected during the Characterizing Atmospheric-Oceanic Parameters of SOARS (Scripps Ocean-Atmosphere Research Simulator) campaign. SOARS is a 36 m-long wave channel (width: 2.5, height: 2.5 m) filled with filtered seawater (approximately 100,000 L) taken in from the ocean at the Scripps pier (Scripps Institution of Oceanography (SIO), La Jolla, CA).[43] SOARS allows for SSA to be produced under controlled conditions such as wave amplitude, wind, and temperature. Nascent SSA was generated through wave breaking (waves of 0.5 m amplitude produced by a totally enclosed, fan-cooled with an electric motor paddle). Individual SSA particles were collected by using a Nano Micro Orifice Uniform Deposit Impactor (nanoMOUDI, MSP Corp., Model 125-R). The air sampling was conducted at a flow rate of 10 lpm at wind speeds of 10 and 19 ms^{-1}. SSAs were substrate-deposited via a home-built silica bead dryer (ca. 50% relative humidity). The samples were deposited onto clean silica wafers and CaF_2 substrates.[44,45]

ATR-FTIR Spectroscopy

The ATR-FTIR data were collected by using a Nicolet iS10 FTIR spectrometer (Thermo Fischer Scientific) with an MCT-A detector. All spectra shown are an average of 100 scans and a resolution of 4 cm^{-1}, in the spectral range from 725 to 4000 cm^{-1}. Before the sample was measured, a background spectrum of the clean AMTIR crystal (with no sample) was first measured. The crystal with the deposited thin film was then measured under the same conditions. Each spectrum was processed (background corrected and CSV exported) by using the OMNIC software and plotted in Origin.

AFM-IR Spectroscopy

A nanoIR2 (Bruker Anasys, Santa Barbara, CA) was equipped with a QCL laser to collect the AFM-IR data. Images and PTIR spectra of each compound deposited on silica substrates were collected in tapping AFM-IR mode, using a gold-coated silicon nitride probe (Bruker), with tip radii of ~30 nm, a resonant frequency of 75 ± 15 kHz, a spring constant of 1 to 7 N/m, and a scan rate within the range of 0.5−0.8 Hz. All images were 40 × 40 μm and collected at a resolution of 512 pixels. All spectra were measured using s-polarized light with a resolution of 2 cm^{-1} over the spectral range extending from 800 to 1800 cm^{-1}. PTIR spectra were processed with the Analysis Studio software (Anasys instrument); images were processed with Gwyddion software and plotted in Origin.

O-PTIR and Micro-Raman Spectroscopy

O-PTIR and micro-Raman spectroscopic data were collected using a mIRage infrared + Raman microscope system (Photothermal Spectroscopy Corp., Santa Barbara, CA) equipped with two mid-IR tunable lasers: a quantum cascade laser (QCL), with a spectral resolution of 6 cm^{-1}, and an optical parametric oscillator (OPO) laser, with a spectral resolution of 4 cm^{-1}. This instrument acquires IR and Raman spectra simultaneously using a visible laser (532 nm probe beam), which is colinear to the IR laser beam. When the IR light is resonant with a vibrational transition, the light is absorbed by the sample and causes local heating in that region. This leads to a thermal lensing effect with a change in the local refractive index that impacts the propagation of the probe beam intensity and gives rise to the O-PTIR signal. In addition to the O-PTIR signal, the visible laser can be used for Raman spectroscopy. This is done by directing a portion of the scattered light into a monochromator and CCD detector. Most importantly, the visible light determines the spatial resolution, which is on the order of 0.5 μm.

CaF_2 substrates were placed inside the instrument, adjusting the focus of the instrument while collecting images at low (10×) and high (40×) magnification. O-PTIR spectra were collected from 755 to 1855 cm^{-1} with a QCL laser and from 2600 to 3600 cm^{-1} with an OPO laser. It should be noted that IR laser power (ranging from 10 to 100%) and probe power (from 2.4 to 40%) were optimized for each sample. The micro-Raman spectra were collected in the spectral range from 700 to 4000 cm^{-1}, with a probe power of 5−100% and an integration time of 1−10 s. All spectra reported were acquired using s-polarized light at a resolution of 2 cm^{-1}. Each spectrum was processed using the mIRage infrared + Raman microscope system PTIR Studio software and plotted with Origin. Raman spectra were baseline corrected.

Pearson Correlation Coefficient (*r*)

Pearson correlation coefficients were used to compare the IR spectra collected with the different infrared methods: ATR-FTIR spectroscopy, AFM-IR spectroscopy, and O-PTIR spectroscopy. The Pearson correlation coefficient is commonly used to assess the linear strength or association of these two variables.[46] This value can range from −1 to 1, where the variables have a perfect correlation when the value is −1 or 1 (indicating a decrease or increase in proportion) and values closer to 0 indicate low or no correlation. Pearson correlation coefficients have been used previously as a similarity parameter to compare the Raman spectra of unknown compounds with the Raman spectra from a spectral database.[36] It was used here to compare similarities of the normalized intensities of the IR spectra (intensity values were normalized between 0 and 1) of different lipids collected with the various spectroscopic techniques used. Therefore, the Pearson correlation was chosen because of an expectation of a high degree of linearity between the intensities and frequencies of rational assignments the different infrared methods and to test whether in fact there is linearity, unlike the Spearman correlation. Both methods have their respective strengths and limitations, they generally provide a similar and accurate measure of the degree of agreement between spectra.[47]

The Pearson correlation coefficient, *r*, was calculated using eq 1:

$$r = \frac{\sum_{800\ cm^{-1}}^{n} (X_i - \overline{X})(Y_i - \overline{Y})}{\sqrt{\sum_{800\ cm^{-1}}^{n} (X_i - \overline{X})^2} \sqrt{\sum_{800\ cm^{-1}}^{n} (Y_i - \overline{Y})^2}} \quad (1)$$

where X_i is the intensity at a wavenumber in the IR spectra of a compound for the first technique, Y_i is the intensity at a wavenumber in the IR spectra of a compound for the second technique, $\overline{X}$ is the average of intensities across the IR spectra of a compound for the first technique, $\overline{Y}$ is the average of intensities across the IR spectra of a compound for the second technique. Spectra of the different samples from the O-PTIR and AFM-IR spectroscopies were then compared to the ATR-FTIR spectra. The initial starting point for this comparison was 800 cm^{-1}. ATR-FTIR and O-PTIR spectra were compared from 800 to 1800 and from 2700 to 3580 cm^{-1}. Comparisons with AFM-IR with the other techniques were done from 800 to 1800 cm^{-1} because higher wavenumber values were not collected with this technique.

Identifying Compounds in SSA and Hyperspectral Mapping

SSA particles collected from SOARS were deposited onto quartz and CaF_2 substrates (stages 4−6) and then analyzed with the mIRage + Raman system. Hyperspectral maps with submicron resolution were also generated to investigate heterogeneities within selected particles. An array of points is mapped across the particle of interest, and O-PTIR and Raman spectra are acquired at each point. After acquiring the spectra, a specific wavenumber of interest can be selected. This wavenumber is selected based on the functional groups present in the samples. The hyperspectral maps are generated using the PTIR software, which produces a color-coded representation. In these maps, regions corresponding to a stronger signal are shown in red, while weaker signals are depicted in blue. For each particle selected, a hyperspectral map was acquired using a spatial interval ranging from 0.2 to 0.5 μm. After data collection, spectra were processed using

https://doi.org/10.1021/acsmeasuresciau.4c00033
ACS Meas. Sci. Au XXXX, XXX, XXX−XXX

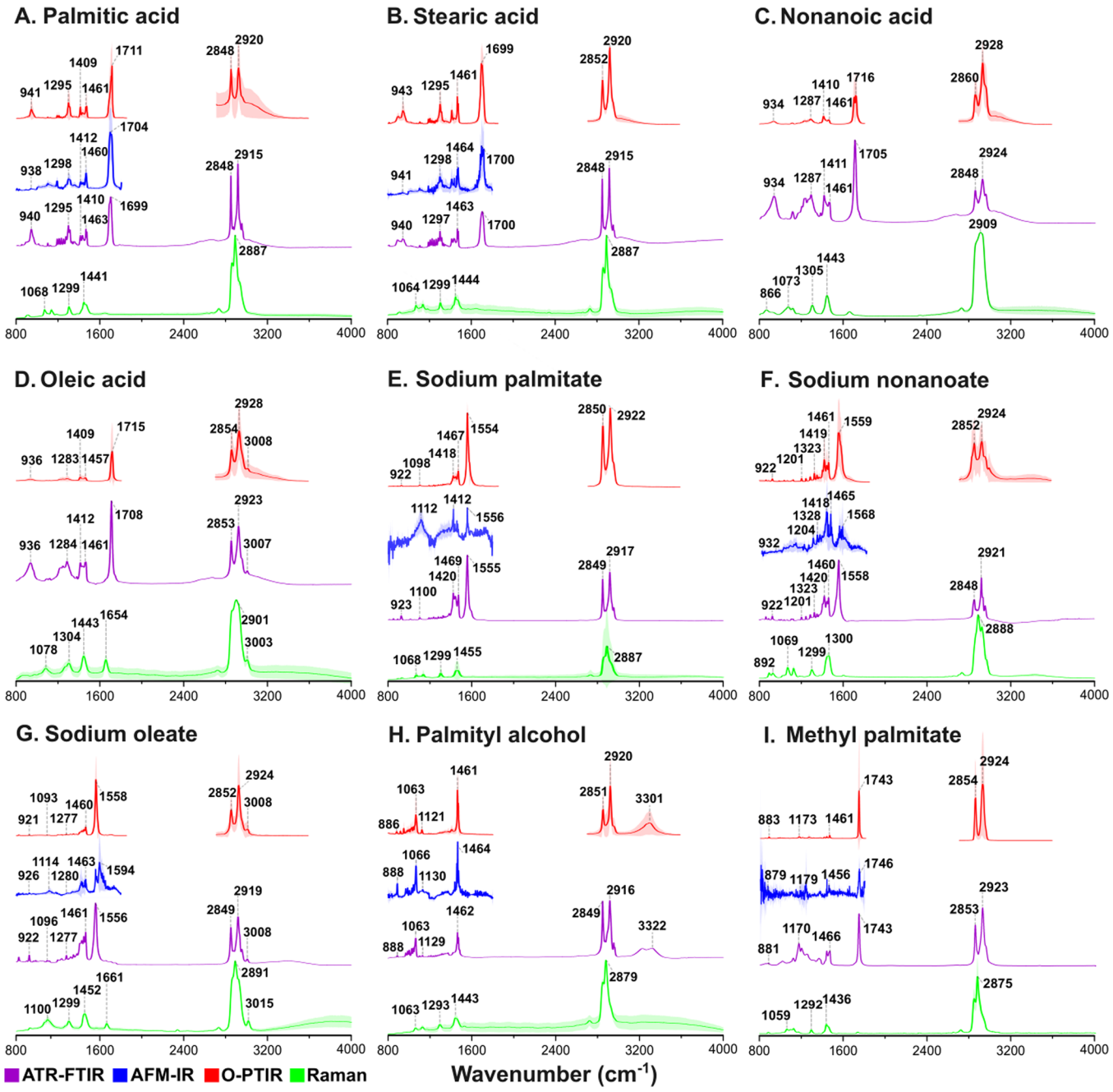

Figure 1. ATR-FTIR (purple), AFM-IR (blue), and O-PTIR (red) spectra of thin films of different lipids ((A) palmitic acid; (B) stearic acid; (C) nonanoic acid; (D) oleic acid; (E) sodium palmitate; (F) sodium nonanoate; (G) sodium oleate; (H) palmityl alcohol; (I) methyl palmitate). AFM-IR spectra were collected for all lipids except nonanoic and oleic acid; see text for further details. The shading shown in some spectra demonstrates differences in intensity measured when the laser was focused on different regions within the same thin film.

PTIR Studio software, plotted within Origin, and compared with the analyzed standards (vide infra) to identify compounds in the sample.

RESULTS AND DISCUSSION

Comparison of Different Vibrational Spectroscopic Probes (ATR-FTIR, AFM-IR, O-PTIR, and Raman) of Some Common Lipids

Figure 1 shows the ATR-FTIR, AFM-IR, O-PTIR, and micro-Raman spectra of various lipid types of different carbon chain lengths including saturated and unsaturated carboxylic acids, saturated and unsaturated carboxylate salts, alcohols, and esters. The shading for some of the spectra collected using microspectroscopic probes shows differences in intensity depending on the exact location of the sample in which the spectrum is measured due to differences in film thickness and light−matter interactions (vide infra). These spectra are organized by first, saturated fatty acids of different chain lengths, unsaturated fatty acid (A−D), sodium salts of saturated and unsaturated fatty acids (E−G), fatty acid alcohols (H), and fatty esters (I). A summary of different vibrational modes and their frequencies for lipids are provided in Table 1.[48−55]

Several differences can be observed when comparing the infrared spectra of the various lipids, starting with the

https://doi.org/10.1021/acsmeasuresciau.4c00033
ACS Meas. Sci. Au XXXX, XXX, XXX−XXX

Table 1. Summary of the Vibrational Assignments for Different Classes of Lipids

	infrared	Raman
vibrational assignments[a] (refs 48−55)	wavenumber (cm^{-1})	wavenumber (cm^{-1})
$\delta(CH_3)$, $\rho(CH_3)$	800−900	800−920
νC−C	849−855	
δ(=C−H)		972
ν_{op}(C−C)	850−1150	1060−1065
ν(C−C)		1080−1110
ν_{ip}(C−C)		1120−1135
ν(C−O)	acids: 1075−1120	1060
	alcohol: 1060−1070	
	esters: 1170−1190	
$r(CH_2)$		1171
δ_{ip}(=CH)		1250−1280
$w(CH_2)$	1180−1340	
$\tau(CH_2)$	1330−1400	1295−1305
$\delta_s(CH_3)$	1350−1370	
$\nu_s(COO^-)$	1423	
δ_{ip}(C−OH)	1431	
$\delta(CH_2)$, $\rho(CH_2)$	1460−1480	1400−1500
$\delta_{sc}(CH_2)$	acids: 1464, 1472	1400−1500
	alcohol: 1464, 1472	
	carboxylates: 1459, 1473	
$\nu_{as}(COO^-)$	carboxylates: 1550−1560	
ν_s(C=O)	acids: 1700−1710	1730−1750
	esters: 1730−1740	
ν(C=C)		1640−1680
$\nu_s(CH_3)$	acids: 2872−2875	2920−2930
	carboxylates: 2850−2874	
$\nu_{as}(CH_3)$	acids: 2920, 2960−2956	
	carboxylates: 2850−2856	
$\nu_s(CH_2)$	2850−2860	2840−2880
$\nu_{as}(CH_2)$	2934−2919	2900−2910
$\nu_s(CH_3)$	2900−2950	2890−2960
$\nu_{as}(CH_3)$	2950−2980	2940−2970
ν(=C−H)	3000−3025	3000−3025
ν(OH)	3200−3800	3200−3800

[a] ν, stretching; ν_{as}, antisymmetric stretching; ν_s, symmetric stretching; ν_{op}, out-of-plane stretching; ν_{ip}, in-plane stretching; δ, bending; δ_s, symmetric bending; δ_{ip}, in-plane bending; δ_{sc}, scissoring bending; ρ, rocking; τ, twisting; and w, wagging.

monoacids. Stearic and palmitic acids form thin solid films, whereas oleic and nonanoic acids were measured in the liquid state, reflecting their phase under ambient conditions (which represent the phase state in which they might be for SSA). Previous studies have demonstrated that spectral shifts and intensities are seen for lipids in solution compared to the solid state[48,49]

The ν_s(C=O) stretching motion is the most intense band for all three infrared spectra (ATR-FTIR, O-PTIR, and AFM-IR) in the 800−1800 cm^{-1} region for the saturated and unsaturated protonated acids. This peak at around 1700 cm^{-1} indicates the protonated state of the carboxylic acid group and can be easily distinguished with infrared spectroscopy. In the case of micro-Raman spectroscopy, this peak is not readily apparent in the spectra, especially for the longer-chain fatty acids. For oleic acid, there is a peak in the micro-Raman spectrum at 1654 cm^{-1} due to the ν(C=C) stretching motion, indicative of an unsaturated fatty acid. This peak is not evident in the infrared spectra. However, the olefinic (C−H) stretch is evident in the infrared and Raman spectra, indicating an unsaturated fatty acid.

Other saturated and unsaturated fatty acid peaks include (C−H) stretching vibrational modes in the spectral regions ranging from 2850 to 2900 cm^{-1} and from 2919 to 2970 cm^{-1}. These are due to methyl and methylene symmetric and asymmetric stretching vibrations ($\nu_{as}(CH_3)$ between 2956 and 2973, $\nu_{as}(CH_2)$ between 2919 and 2947 cm^{-1}, $\nu_s(CH_3)$ between 2872 and 2900 cm^{-1}, and $\nu_s(CH_2)$ between 2850 and 2876 cm^{-1}). These peaks can provide information related to the carbon chain length. For chains shorter than ten carbons, these peaks exhibited lower intensity ratios of methylene over methyl. However, as the chain length increases, the (CH_2) stretching peak intensities also increase, increasing the ratio. ATR-FTIR is particularly useful in observing carbon chain length trends as it can simultaneously measure low and high frequencies under the same conditions. Comparing spectra with AFM-IR and O-PTIR may pose challenges due to potential variations in laser power and AFM tip interactions with the sample.[52] Raman spectroscopy also allows us to compare the number of carbons in the chain based on the intensities of the peaks related to $\nu(CH_2)$ and $\nu(CH_3)$ vibrations at 2850 and 2935 cm^{-1}, respectively.[53]

Peaks in these spectra associated with bending, $\delta(CH_2)$, and rocking, $\rho(CH_2)$, modes of methylene groups were observed for thin films at 1462 and 1472 cm^{-1}, respectively. It has been observed that for compounds with less than 12 carbons, $\delta(CH_2)$ and $\rho(CH_2)$ peaks are red-shifted, for carbon chains above 12 carbons, this shift becomes less significant.[54] Another region of interest for distinguishing between linear monoacids is the spectral region between 1180 and 1340 cm^{-1}, corresponding to the w(CH_2) and $\tau(CH_2)$ vibrations. In this region, stearic acid showed an additional peak compared to palmitic acid (ca. at 895 cm^{-1}) following the "rule of two" that has been previously proposed for even-numbered carbon chains.[55] This rule indicates that the number of observed peaks will equal the number of carbons in the chain divided by 2. This additional peak is expected since stearic acid has two more carbons in its chain (C18) than palmitic acid (C16). However, this method only applies to thin film samples with chain lengths between 10 and 26 carbons.[55] When the lipid is in a liquid state, peaks can be less resolved and peaks can shift in frequency, e.g., there is a more intense peak at 1380 cm^{-1} that is absent in solid films, which can possibly be used to distinguish the phase state of these compounds in complex environmental samples.

For the sodium carboxylate salts, most evident in all of the infrared spectra across the three techniques is the loss of the (C=O) for the protonated carboxylic acid and instead is replaced by the asymmetric and symmetric carboxylate (COO^-) stretching motion around 1555 and 1460 cm^{-1}, respectively. It has been observed that $\nu_{as}(COO^-)$ and $\nu_s(COO^-)$ vary depending on the cation present, with a difference of 40 cm^{-1}, and bidentate coordination may exhibit split peaks.[54] All other vibrational frequencies are mainly close to what they were in the protonated state. This change in protonation state is not evident for micro-Raman spectroscopy, as these absorptions, which distinguish (−COOH) from ($-COO^-$) are very weak in Raman spectroscopy. Instead, the protonated and deprotonated forms have nearly identical spectra, making infrared spectroscopy an important probe for the protonation state of fatty acids.

https://doi.org/10.1021/acsmeasuresciau.4c00033
ACS Meas. Sci. Au XXXX, XXX, XXX−XXX

When comparing monoacids with a saturated fatty alcohol (palmityl alcohol, Figure 1H) and a fatty ester (methyl palmitate, Figure 1I), the saturated alcohols exhibited a peak in the infrared spectra around 3300 cm^{-1} due to the (O−H) stretching mode. For the ester, (C=O) is the most intense peak in the infrared spectra with a peak around 1745 cm^{-1}, which is shifted by ca. 40 cm^{-1} from the (C=O) of the fatty acid. Although these two distinguishing peaks are evident in the infrared spectra, they are too weak to be seen in the Raman spectrum.

The ν(C−O) vibrational mode also differs from the liquid to solid phases. Monoacids in the liquid phase peaked around 1100 cm^{-1}, in the solid phase, they blue-shifted to 1110−1120 cm^{-1}. In the case of carboxylates, they exhibit this vibrational mode at the exact wavenumber of their corresponding acid. However, in the alcohols, this peak appears at a lower wavenumber (1060−1070 cm^{-1}), whereas for esters, it is red-shifted (1170−1190 cm^{-1}).

The results above indicate for IR spectroscopy that the peak frequencies, depending on the specific vibrational mode analyzed, allow for easier identification of lipid types than micro-Raman spectroscopy, which has limitations compared to IR spectroscopy in distinguishing between different types of lipids (acid, sodium salt, alcohol, or ester). However, micro-Raman spectroscopy is very useful for determining saturated versus unsaturated fatty acid forms, as the (C=C) stretching motion is evident. Infrared spectroscopy can also be used by the appearance of the olefinic (C−H) stretch. When analyzing complex mixtures due to the matrix effect and other compounds that may exhibit similar peaks and varying intensities, it is important to understand the strengths and weaknesses in identifying and characterizing lipid compounds using micro-Raman spectroscopy.

Correlation of Different Infrared Spectroscopies of Some Common Lipids

As noted above, infrared spectroscopy can be useful in differentiating lipids and, in some cases, their phase state. Evident in Figure 1 is that there are differences between the three infrared methods, especially comparing AFM-IR to ATR-FTIR and O-PTIR spectroscopy. Our interest in utilizing Pearson's correlation coefficient to determine the degree of linearity between these techniques and to quantitatively evaluate these differences; Pearson correlation coefficients and scatter plots between techniques (ATR-FTIR/O-PTIR, ATR-FTIR/AFM-IR, AFM-IR/O-PTIR) for normalized spectral intensities (range from 0 to 1) for a few of the different lipids were determined (Table 2 and Figure 2). At least 500 intensities (at $n > 500$ wavenumbers) were compared, obtaining significant correlation coefficients ($p < 0.05$). This analysis was done for solid samples where all three measurements (ATR-FTIR, O-PTIR, and AFM-IR) were made. These include spectra collected for palmitic acid, stearic acid, sodium palmitate, sodium nonanoate, sodium oleate, palmityl alcohol, and methyl palmitate.

Pearson correlation coefficients between these methods ranged from 0.287 to 0.901 between ATR-FTIR, AFM-IR, and O-PTIR. For the saturated fatty acids (palmitic acid and stearic acid), the techniques showed some of the highest correlations (above 0.84), indicating similarities in peak location (wavenumbers) and proportion of peak intensities between techniques. This suggests that any technique used to measure these long-chain fatty acids would provide spectra suitable for the identification or quantification. Sodium salts (Figure 2B) exhibited high Pearson correlation coefficients between ATR-FTIR and O-PTIR (above 0.84), whereas AFM-IR showed lower correlations with the other techniques. Specifically, for sodium nonanoate, Pearson correlations were 0.67 for ATR-FTIR/AFM-IR and 0.62 for O-PTIR/AFM-IR, while for

Table 2. Pearson Correlation Coefficients between Techniques (ATR-FTIR/O-PTIR, ATR-FTIR/AFM-IR, and AFM-IR/O-PTIR) for Intensity-Normalized Spectra for Different Lipids

Pearson correlation[a]	ATR-FTIR/O-PTIR	ATR-FTIR/AFM-IR	O-PTIR/AFM-IR
palmitic acid	0.843	0.870	0.882
stearic acid	0.896	0.845	0.848
sodium palmitate	0.883	0.414	0.363
sodium nonanoate	0.841	0.668	0.621
sodium oleate	0.844	0.426	0.442
palmityl alcohol	0.877	0.845	0.805
methyl palmitate	0.901	0.348	0.287

[a]All correlations were significant ($p < 0.05$) and were estimated using at least 500 values ($n > 500$).

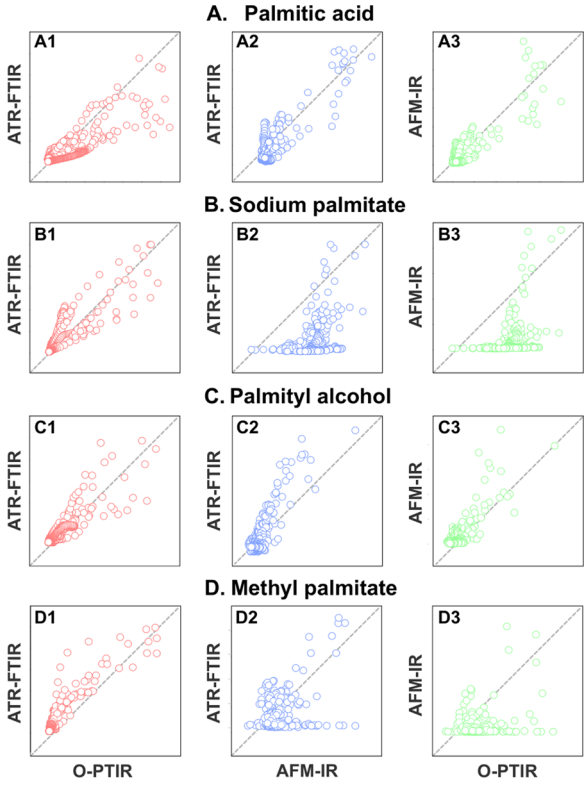

Figure 2. Scatter plots showing similarities for normalized spectral intensities (0−1) between techniques (ATR-FTIR/O-PTIR—red; ATR-FTIR/AFM-IR—blue, and AFM-IR/O-PTIR—green). For these calculations, the value of 1 was assigned to the most intense peak within the frequency range from 800 to 4000 cm^{-1} for ATR-FTIR/O-PTIR and from 800 to 1800 cm^{-1} for ATR-FTIR/AFM-IR and AFM-IR/O-PTIR) for four of the different lipids analyzed: (A) palmitic acid; (B) sodium palmitate; (C) palmityl alcohol, and; (D) methyl palmitate. Wavenumber values are distributed from less intense (closer to 0) to more intense (closer to 1) by the technique on the *x*axis. The 1:1 line is shown when there is complete agreement of normalized intensities between techniques and the Pearson correlation coefficient is equal to one.

https://doi.org/10.1021/acsmeasuresciau.4c00033
ACS Meas. Sci. Au XXXX, XXX, XXX−XXX

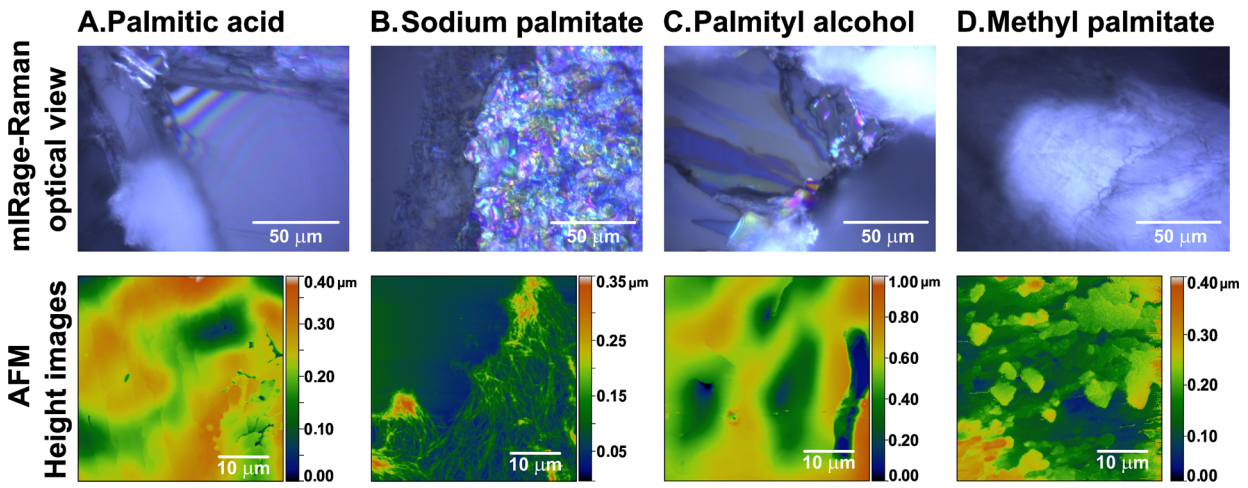

Figure 3. mIRage-Raman optical view (upper panel) and AFM height images (lower panel) for thin films of (A) palmitic acid; (B) sodium palmitate; (C) palmityl alcohol; and (D) methyl palmitate.

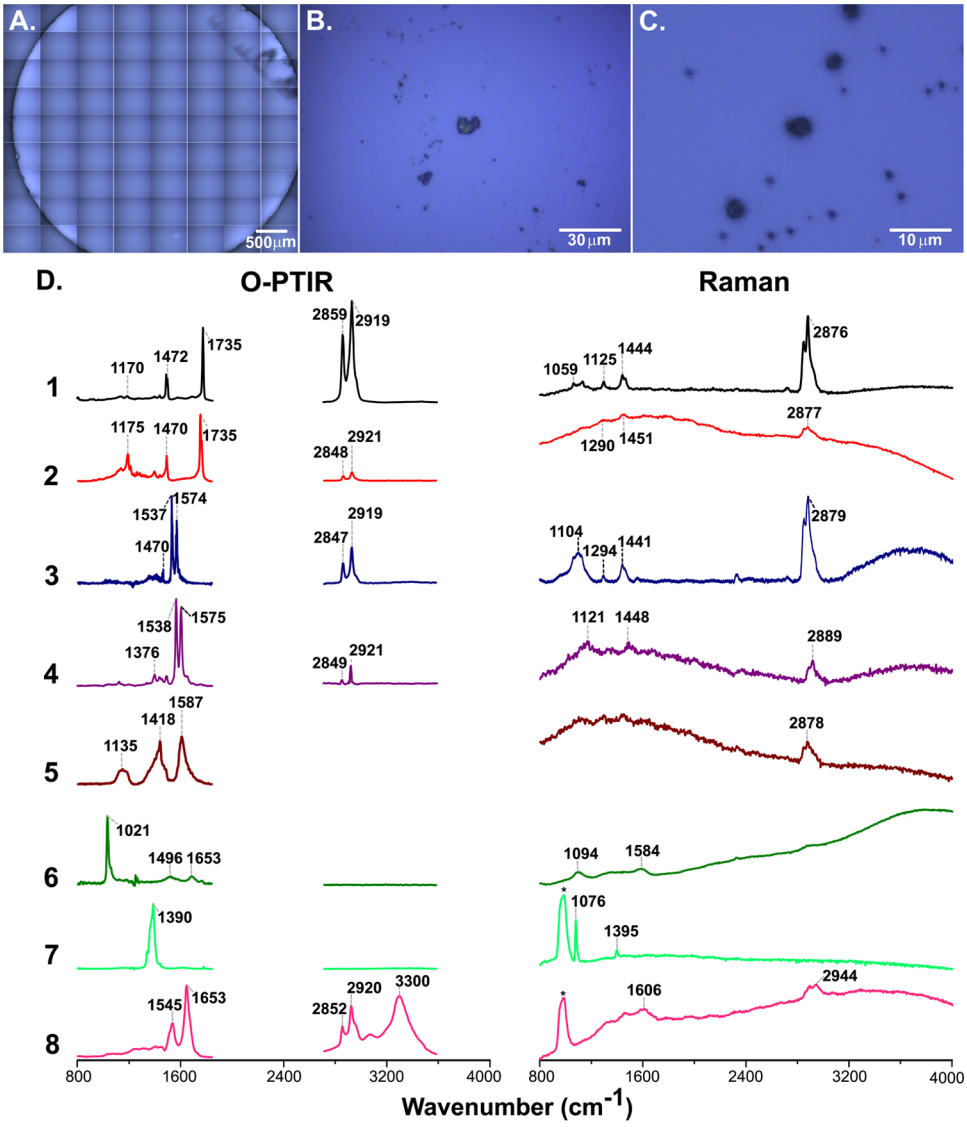

Figure 4. Examples of mIRage-Raman images of SSA particles on CaF_2 substrate ((A) CaF_2 substrate low magnification mosaic image collection; (B) 10× magnification; (C) ×40 magnification). (D) O-PTIR and micro-Raman spectra of individual SSA particles. The OPO laser was not used for particle 5. For particles labeled 1 through 6, a CaF_2 substrate was used. For particles labeled 7 and 8, a silicon wafer with an oxide layer was used, and asterisks denote peaks present due to the substrate.

https://doi.org/10.1021/acsmeasuresciau.4c00033
ACS Meas. Sci. Au XXXX, XXX, XXX−XXX

sodium palmitate and sodium oleate, they were below 0.44. These two compounds showed a lower correlation for wavelengths below 1400 cm^{-1} having a more intense peak around 1112 cm^{-1} than the other techniques, related to a broader peak for the ν(C−O) vibrational mode. In the scatter plot, the deviation from the 1:1 proportion line and in the collected spectra, higher intensities were observed for the other techniques. In contrast, the intensities were lower for AFM-IR with higher noise levels (lower S/N). Thin films for carboxylates may have heterogeneities evident on the nanoscale (e.g., coordination mode and crystallinity), leading to these lower correlation values.

For palmityl alcohol (Figure 2C), the Pearson correlations were higher than 0.81, showing good agreement among techniques. However, the correlation between AFM-IR spectra and spectra from the other infrared techniques was the lowest. Methyl palmitate (Figure 2D), a representative fatty ester compound, with spectra collected by ATR-FTIR and O-PTIR, showed a high Pearson correlation (0.90). In comparison, correlations with AFM-IR were lower than 0.35. For this compound, it was observed that the methyl palmitate thin film deposited on the silica substrate would melt while the spectra were collected in tapping mode, making it challenging to detect the changes on the surface and hence the refractive index even when the IR laser power was decreased. The melting point of methyl palmitate falls slightly higher than ambient temperatures (32 °C) and is lower than other types of compounds with the same number of carbons (palmitic acid at 62.9 °C; sodium palmitate: from 283 to 290 °C; palmityl alcohol at 49.3 °C).[55] This highlights a potential limitation of the AFM-IR technique as it is difficult to measure liquids (leading to increased probe contamination) and compounds with lower melting points. This limitation is particularly relevant for studying SSA, which has different mixing states and compounds with varying physicochemical properties.

Overall, there are some limitations of AFM-IR spectroscopy compared to O-PTIR spectroscopy due to several factors including sample tip interactions and the lack of correlation in peak intensities compared to spectra collected using traditional infrared spectroscopy methods that most standard spectral libraries are based upon. In addition, polarization effects due to crystalline orientation can contribute to spectra variation for these laser-based microspectroscopic probes.[56−59]

While O-PTIR spectroscopy can measure particles at the submicron scale, on the order of 500 nm, it is AFM-IR spectroscopy that provides a better understanding of the sample topography by generating height images offering more information about the morphology of the sample. This technique can resolve nanoscale features, improving the evaluation of the sample's heterogeneity. Height images from AFM-IR showed that thin films have a thickness between 0.35 and 1 μm (representative of height variability for regions analyzed on substrate), providing quantifiable insight into how these compounds may assemble on a surface. Figure 3 displays images obtained with the mIRage-Raman for O-PTIR (optical view) and nanoIR2 for the AFM-IR (height images) of thin films for (A) palmitic acid, (B) sodium palmitate, (C) palmityl alcohol, and (D) methyl palmitate. Compared to the other techniques, one major advantage of AFM-IR spectroscopy is its ability to analyze samples with nanoscale resolution. However, as previously observed, if the primary focus is chemical characterization and the sample features analyzed are just below microns in dimension, the O-PTIR spectroscopy provides an alternative to AFM-IR spectroscopy.

O-PTIR and Raman Spectroscopy of Select Substrate-Deposited Sea Spray Aerosols (SSAs) Collected from the Scripps Ocean-Atmosphere Research Simulation (SOARS) Facility

SOARS, a unique ocean-atmosphere facility, can produce SSAs over a range of conditions and with a range of different compositions, viscosity and size.[60,61] Here we utilize O-PTIR and micro-Raman spectroscopy with imaging capabilities to identify different compounds and the distribution of these compounds within SOARS collected single SSA particles.

Figure 4 shows images (A, C) collected at different resolutions of SSAs deposited on CaF_2 substrates. It can be seen in the images, especially the highest resolution image (Figure 4C), that individual particles are deposited on the substrate. Once a particle was identified, the spectra of the O-PTIR and Raman were recorded in the center of that particle. Eight representative spectra collected for individual particles are shown in Figure 4D (particles labeled 1 through 8). The identification of these spectra was made possible by using the spectral library generated for some of the lipids in Figure 1 and other compounds that have been measured (as shown in the SI). These SI reference spectra include a variety of compounds (Figure S1—bovine serum albumin (BSA) protein; Figure S2—dipalmitoylphosphatidylcholine (DPPC); Figure S3—fulvic acid; Figure S4—glucose; Figure S5—sodium salt of humic acid; Figure S6—laminarin; Figure S7—lipopolysaccharide (LPS); Figure S8—oxalic acid; Figure S9—sodium alginate; Figure S10—sodium nitrate; Figure S11—sodium oxalate; Figure S12—sodium sulfate; and Figure S13—sucrose).

Particles 1 and 2 were identified as a fatty ester, methyl palmitate. It is possible to observe the ν(C=O) vibrational mode at 1735 cm^{-1}, methylene vibrations ($\delta(CH_2)$, $\rho(CH_2)$, $\delta_{sc}(CH_2)$, $\nu_s(CH_2)$, and $\nu_{as}(CH_2)$) between 1380 and 1480 cm^{-1}, 2850 and 2919 cm^{-1}, and the ν(C−O) vibrational mode at 1170 cm^{-1} characteristic of methyl esters. The difference between those particles is that the Raman spectra for Particle 2 showed fluorescence, while Particle 1 did not. This suggests that the presence of additional light-absorbing compounds in Particle 2 gives rise to the fluorescence background for Particle 2. Furthermore, both Raman spectra exhibited peaks observed previously for methyl esters (1060, 1290, 1450, and 2880−2890 cm^{-1}).

Particles 3 and 4 show peaks around 1538 and 1574 cm^{-1} assigned to the $\nu_{as}(COO^-)$ vibrational mode. These peaks are indicative of carboxylate salts, and the two large intensity peaks above 1525 cm^{-1} suggest more than one salt is present in the particle or that the divalent cation, i.e., calcium carboxylates, is present as these show a doublet around 1542 and 1579 cm^{-1}.[62] Most importantly, there is evidence for the deprotonation state. The Raman spectra of Particle 3 show the typical spectra observed for fatty acids, alcohols, and esters, giving no additional information about the lipids present. Peaks corresponding to the vibrational modes, ν(C−C): 1000−1120 cm^{-1}, 1294 cm^{-1}, $\delta(CH_2)$ and $\nu(CH_2)$ 1440−1450 cm^{-1}, and ν(C−H): 2880−2890 cm^{-1} were also observed in carboxylate Raman spectra. Particle 4 shows fluorescence, indicating light-absorbing components present in the particle.

Particle 5 has 1135, 1418, and 1587 cm^{-1}, similar to those observed in humic acid salts (1031, 1383, and 1581 cm^{-1}

https://doi.org/10.1021/acsmeasuresciau.4c00033
ACS Meas. Sci. Au XXXX, XXX, XXX−XXX

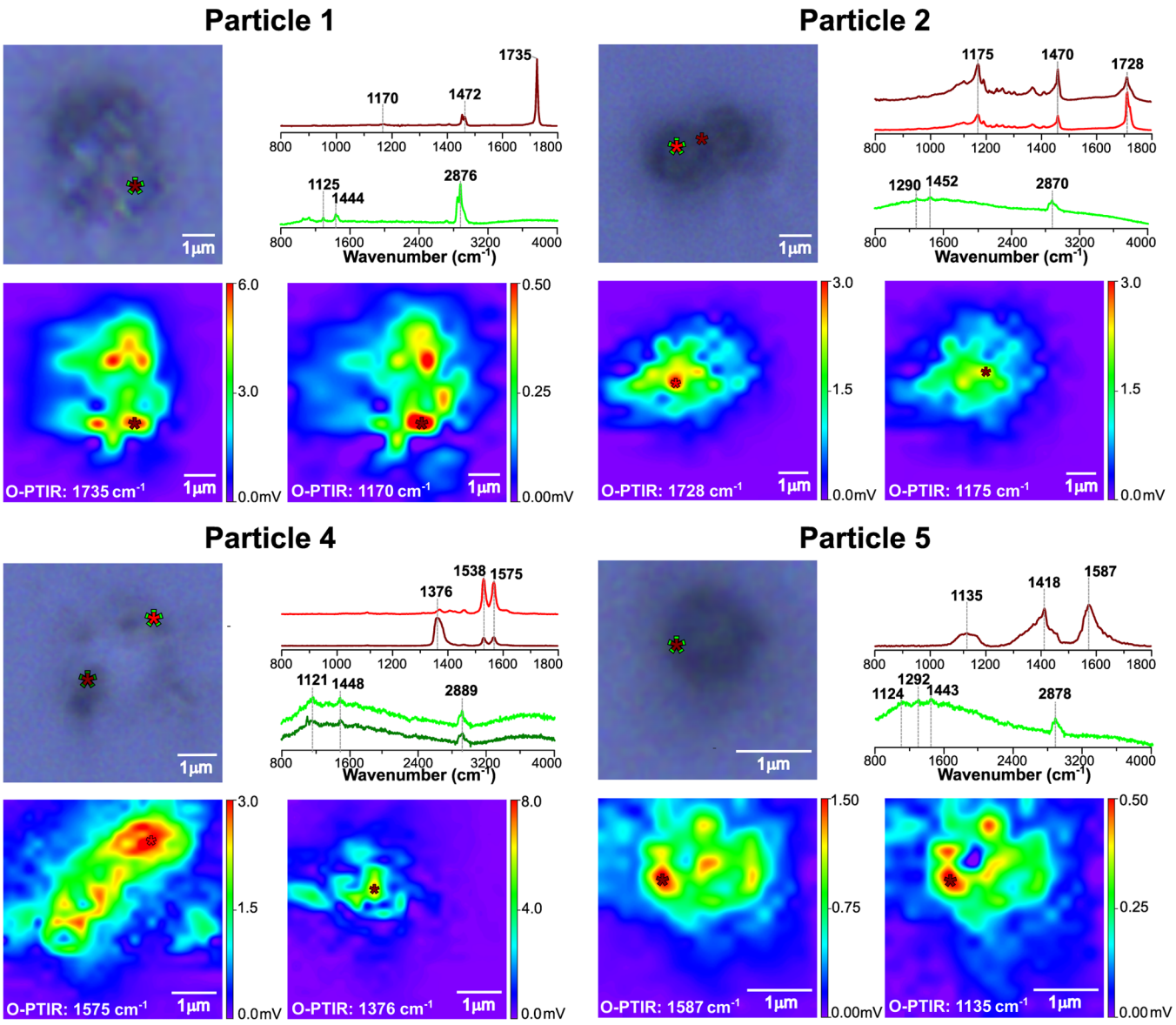

Figure 5. Optical images; O-PTIR spectra (fingerprint region: 800−1800 cm^{-1}), micro-Raman spectra (ranging from 800 to 4000 cm^{-1}), and hyperspectral mapping of O-PTIR spectroscopy ($\nu(COO^-)$ and $\nu(C{=}O)$ from 1580 to 1725 cm^{-1}; $\nu(C{-}O)$ from 1135 to 1175 cm^{-1} and $\nu_{as}(NO_3)$ at 1376 cm^{-1}) for particles labeled 1, 2, 4, and 5 from Figure 4. The locations where the spectra were taken are indicated by a red asterisk (O-PTIR) and a green circle (Raman).

broad peaks, Figure S5). Those peaks can be assigned to $\nu(C{-}O)$, methylene vibrations ($\delta(CH_2)$, $\rho(CH_2)$, $\delta_{sc}(CH_2)$, $\nu_s(CH_2)$), $\nu(C{=}C)$ of aromatic groups, and $\nu(C{=}O)$.[62] Due to the complex mixture and molecular structure of this particle, including light-absorbing components, the Raman spectra collected for both the standard in SI and Particle 5 exhibited fluorescence.

Particles 6 and 7 are representative of inorganic compounds. Particle 6 revealed a predominant peak at 1021 cm^{-1} that was attributed to $\nu_{as}(SO_4^{2-})$. Phase state, crystallinity, and coordination mode all impact the frequency of the sulfate peak as well as the hydration state of the salt.[63] Particle 7 exhibited a peak that matches nitrate IR vibrational modes with a peak at 1390 cm^{-1} ($\nu_{as}(NO_3^-)$: 1345−1380 cm^{-1}), which is consistent with the Raman spectra that showed a high-intensity peak at 1076 cm^{-1} due to the more Raman active $\nu_s(NO_3^-)$.[64] Finally, Particle 8 represented spectra characteristic of biological compounds such as proteins. It exhibited intense peaks at 1545, 1653, 2852, 2920, and 3300 cm^{-1}. These peaks resembled those of bovine serum albumin. Specifically, the peaks could be assigned to amide II, $\nu(C{-}N)$, and $\delta(N{-}H)$ around 1550 cm^{-1}, and amide A peak for $\nu(N{-}H)$ near 3500 cm^{-1}.[65]

Three out of the eight particles yielded fluorescence-free Raman spectra, however, these same particles show O-PTIR clear spectral features. Given that SSA samples are complex and contain a high proportion of biological components, difficulties in this analysis are expected and have been discussed previously for SSA particles.[19] Therefore, the ability to collect IR and Raman spectra simultaneously helps enhance the accuracy of compound identification for individual particles, as they operate as complementary techniques.

Chemical Maps of Substrate-Deposited SSAs

Some limitations faced while collecting individual spectra for SSA around or below one micron are that particles can show a

https://doi.org/10.1021/acsmeasuresciau.4c00033
ACS Meas. Sci. Au XXXX, XXX, XXX−XXX

heterogeneous distribution with IR or Raman active compounds. Hyperspectral imaging and chemical mapping can address this issue. This capability is valuable in determining that the spectra collected at a specific point in the particle are (or are not) representative of the particle.

Figure 5 presents the analysis of four selected particles (labeled as 1, 2, 4, and 5 in Figure 4). Figure 5 includes optical images; O-PTIR spectra (800−1800 cm^{-1}), micro-Raman spectra (800−4000 cm^{-1}), and the hyperspectral mapping of O-PTIR spectroscopy focused on some vibrational modes (ν(C=O)—1580−1725 cm^{-1}, ν(C−O)—1135−1175 cm^{-1} and $\nu_{as}(NO_3)$—1376 cm^{-1}). The locations where the spectra were taken are indicated by asterisks for Raman spectra; shown in red and green circles. A higher value can be expected to represent a higher concentration or contribution of the corresponding vibrational mode (red hues are highest, blue hues are lowest). However; it should be noted that changes in laser power can also affect these intensity values so comparisons between particles should be made cautiously.

Particle 1 was identified in methyl palmitate spectra and showed well-defined O-PTIR and Raman spectra. The mapping of the ν(C=O) vibrational mode at 1735 cm^{-1} showed higher intensities than the map for the ν(C−O) vibration at 1170 cm^{-1}, consistent with that observed in the spectra. Additionally, the areas within the particle that exhibited higher intensities for both vibrational modes were colocated in the same regions, suggesting that the particle may be homogeneous. In contrast, Particle 2, which displayed fluorescence in its Raman spectra despite matching methyl palmitate's IR spectra, appears more heterogeneous. Spectra collected from different regions of the particle showed different predominant peaks. Dark red spectra displayed a higher intensity for ν(C−O) (1175 cm^{-1}) while the bright red spectra presented a more intense peak for ν(C=O) (1728 cm^{-1}). This may be due to the light-absorbing compound; which is difficult to identify from these spectra due to either low-intensity peaks or low concentrations.

Particle 4 appears to be an aggregate, exhibiting greater heterogeneity than the other particles. Spectral mapping at 1575 cm^{-1}, a frequency associated with $\nu_{as}(COO^-)$, shows higher intensity in some regions, while spectral mapping at 1376 cm^{-1}, a frequency associated with $\nu_{as}(NO_3^-)$, displayed greater intensity in a different region within the particle. This shows that this particle is a mixture of inorganic and organic compounds, frequently observed in SSAs.[66−68] The Raman spectrum collected of the same particle has a relatively high background and provides less information.

Lastly, Particle 5 contains a high organic content. This aligns with the assignment made for this particle as having a humic-type material. For this particle, the peak at 1586 cm^{-1} can be assigned to ν(C=C) of aromatic groups or $\nu_{as}(COO^-)$, and the peak at 1035 cm^{-1} was assigned to ν(C−O). The maps of both vibrational modes displayed proportional intensities to the collected spectra, indicating that the particle is relatively homogeneous.

CONCLUSIONS

This study employed complementary vibrational spectroscopic probes (ATR-FTIR, AFM-IR, O-PTIR, and micro-Raman) to analyze different thin lipid films and other compounds found in environmental samples, including sea spray aerosols. Understanding the chemical composition of complex environmental samples, such as aerosols, is important if we are to understand their global impacts. For sea spray aerosols, one of their important impacts is through ice nucleation[69] including particles containing lipids.[70] Each of the techniques employed provide valuable information about the spectral characteristics of different lipids and other chemical species. For the lipids, ATR-FTIR and O-PTIR spectroscopy demonstrated a high correlation and effectively identified different lipid types and their protonation states. Given that many vibrational databases are based on more traditional vibrational methods including FTIR spectroscopy, this high correlation is important when analyzing complex environmental samples with O-PTIR spectroscopy. O-PTIR spectroscopy has a number of advantages for analyzing environmental samples relative to FTIR analysis including no need for a reference or background spectrum, submicron resolution, and the ability to analyze both fluorescent and nonfluorescent samples as well as being nondestructive. Although AFM-IR spectroscopy allows for the characterization at higher spatial resolution, the spectra showed a lower correlation due to intensity differences compared to those of more traditional infrared methods. In addition, for softer liquid samples, variable tip−sample interactions and possible tip contamination can also be an issue. Micro-Raman spectroscopy also has submicrometer spatial resolution but does not distinguish between lipid types. However, the Raman spectra provided valuable insights into the presence of light-absorbing compounds.

Overall, combining the techniques of O-PTIR, Raman spectroscopy, and chemical mapping can offer a comprehensive approach to characterizing individual particles in collected sea spray aerosols. This integrated approach improved compound identification accuracy and facilitated the assessment of compound distribution and heterogeneity, thereby enhancing our understanding of the complex nature of sea spray aerosol samples and potentially other environmental samples. Across techniques, the varying selection rules, modes of operation, and thicknesses for each of the films should be considered in evaluating differences in spectral frequencies and intensities. The study presented here addressed several of these issues.

ASSOCIATED CONTENT

Supporting Information

The Supporting Information is available free of charge at https://pubs.acs.org/doi/10.1021/acsmeasuresciau.4c00033.

List of compounds analyzed, CAS number, solvent of stock solution for thin film preparation, and commercial source of compounds purchased, and 13 figures of additional reference spectra of organic and inorganic components of sea spray aerosol (PDF)

AUTHOR INFORMATION

Corresponding Author

Vicki H. Grassian − *Department of Chemistry and Biochemistry, University of California San Diego, La Jolla, California 92093, United States;* orcid.org/0000-0001-5052-0045; Email: vhgrassian@ucsd.edu

Authors

Carolina Molina − *Department of Chemistry and Biochemistry, University of California San Diego, La Jolla, California 92093, United States*

https://doi.org/10.1021/acsmeasuresciau.4c00033
ACS Meas. Sci. Au XXXX, XXX, XXX−XXX

Deborah Kim − *Department of Chemistry and Biochemistry, University of California San Diego, La Jolla, California 92093, United States;* orcid.org/0000-0001-6717-8397
Lincoln Mehndiratta − *Department of Chemistry and Biochemistry, University of California San Diego, La Jolla, California 92093, United States*
Jennie Lee − *Department of Chemistry and Biochemistry, University of California San Diego, La Jolla, California 92093, United States*
Chamika K. Madawala − *Department of Chemistry, University of Iowa, Iowa City, Iowa 52242, United States*
Jonathan H. Slade − *Department of Chemistry and Biochemistry, University of California San Diego, La Jolla, California 92093, United States;* orcid.org/0000-0002-5026-4229
Alexei V. Tivanski − *Department of Chemistry, University of Iowa, Iowa City, Iowa 52242, United States;* orcid.org/0000-0002-1528-2421

Complete contact information is available at: https://pubs.acs.org/10.1021/acsmeasuresciau.4c00033

Notes

The authors declare no competing financial interest.

■ ACKNOWLEDGMENTS

The authors would like to acknowledge support from the National Science Foundation through the Center for Aerosol Impacts on Chemistry of the Environment funded under the Centers for Chemical Innovation Program Grant CHE1801971. The authors also acknowledge that the research reported here was funded in whole or in part by the Army Research Office/Army Research Laboratory via an equipment grant #W911NF2210033 to purchase the mIRage + Raman system at the University of California, San Diego. Any errors and opinions are not those of the Army Research Office or Department of Defense and are attributable solely to the author(s). The authors are very grateful to the CHAOS team and thank Raymond J. Leibensperger III, Ke'La Kimble, Julie Dinasquet, Francesca Malfatti, Christopher Lee, Grant Deane, Dale Stokes and Kimberly A. Prather. We also thank the CAICE engineering and facility members Joseph Mayer and Robert Klidy and the Scripps Institution of Oceanography Marine Science Development Center team, who made the CHAOS campaign a success. Additionally, we thank Dr. Eshani Hettiarachchi for their technical edits and comments.

■ REFERENCES

(1) Zhang, C. C. Chapter 8: UV-Visible and infrared spectroscopic methods in environmental analysis. In *Fundamentals of Environmental Sampling and Analysis*; Wiley Online Library Publishing, 2006; pp 1−436.
(2) Silva, A. B.; Bastos, A. S.; Justino, C. I. L.; da Costa, J. P.; Duarte, A. C.; Rocha-Santos, T. A. P. Microplastics in the environment: Challenges in analytical chemistry - A review. *Anal. Chim. Acta* **2018**, *1017*, 1−19.
(3) Galvão, E. S.; Santos, J. M.; Lima, A. T.; Reis, N. C.; Orlando, M. T. D. A.; Stuetz, R. M. Trends in analytical techniques applied to particulate matter characterization: A critical review of fundaments and applications. *Chemosphere* **2018**, *199*, 546−568.
(4) Ogrizek, M.; Kroflič, A.; Šala, M. Critical review on the development of analytical techniques for the elemental analysis of airborne particulate matter. *Trends in Environmental Analytical Chemistry* **2022**, *33*, No. e00155.
(5) Sharma, S.; Jaiswal, S.; Duffy, B.; Jaiswal, A. K. Nanostructured materials for food applications: spectroscopy; microscopy and physical properties. *Bioengineering* **2019**, *6*, 26.
(6) Li, Y.; Shen, B.; Li, S.; Zhao, Y.; Qu, J.; Liu, L. Review of stimulated Raman scattering microscopy techniques and applications in the biosciences. *Adv. Biol.* **2021**, *5*, No. 2000184.
(7) Gredilla, A.; Fdez-Ortiz de Vallejuelo, S.; Elejoste, N.; de Diego, A.; Madariaga, J. M. Non-destructive Spectroscopy combined with chemometrics as a tool for Green Chemical Analysis of environmental samples: A review. *TrAC, Trends Anal. Chem.* **2016**, *76*, 30−39.
(8) Kim, K.-H.; Kabir, E.; Kabir, S. A review on the human health impact of airborne particulate matter. *Environmental International* **2015**, *74*, 136−143.
(9) Pöschl, U. Atmospheric aerosols: Composition; transformation; climate and health effects. *Angew. Chem., Int. Ed.* **2005**, *44*, 7520−7540.
(10) Fuzzi, S.; Baltensperger, U.; Carslaw, K.; Decesari, S.; Denier Van Der Gon, H.; Facchini, M. C.; Fowler, D.; Koren, I.; Langford, B.; Lohmann, U.; et al. Particulate matter; air quality and climate: lessons learned and future needs. *Atmospheric Chemistry and Physics* **2015**, *15*, 8217−8299.
(11) Moorchilot, V. S.; Aravind, U. K.; Menacherry, S. P. M.; Aravindakumar, C. T. Single-particle analysis of atmospheric aerosols: Applications of Raman spectroscopy. *Atmosphere* **2022**, *13*, 1779.
(12) Wu, L.; Ro, C. U. Aerosol hygroscopicity on a single particle level using microscopic and spectroscopic techniques: A review. *Asian Journal of Atmospheric Environment* **2020**, *14*, 177−209.
(13) Riemer, N.; Ault, A. P.; West, M.; Craig, R. L.; Curtis, J. H. Aerosol mixing state: Measurements; modeling; and impacts. *Reviews of Geophysics* **2019**, *57*, 187−249.
(14) Ault, A. P.; Axson, J. L. Atmospheric aerosol chemistry: Spectroscopic and microscopic advances. *Anal. Chem.* **2017**, *89*, 430−452.
(15) Liang, Z.; Chu, Y.; Gen, M.; Chan, C. K. Single-particle Raman spectroscopy for studying physical and chemical processes of atmospheric particles. *Atmospheric Chemical and Physics* **2022**, *22*, 3017−3044.
(16) Laskin, A.; Gilles, M. K.; Knopf, D. A.; Wang, B.; China, S. Progress in the analysis of complex atmospheric particles. *Annu. Rev. Anal. Chem.* **2016**, *9*, 117−143.
(17) Mael, L. E.; Busse, H.; Grassian, V. H. Measurements of immersion freezing and heterogeneous chemistry of atmospherically relevant single particles with micro-Raman spectroscopy. *Anal. Chem.* **2019**, *91*, 11138−11145.
(18) Eom, H. J.; Gupta, D.; Cho, H. R.; Hwang, H.; Hur, S.; Gim, Y.; Ro, C. U. Single-particle investigation of summertime and wintertime Antarctic sea spray aerosols using low-Z particle EPMA; Raman microspectrometry; and ATR-FTIR imaging techniques. *Atmos. Chem. Phys.* **2016**, *16*, 13823−13836.
(19) Cochran, R. E.; Laskina, O.; Trueblood, J. V.; Estillore, A. D.; Morris, H. S.; Jayarathne, T.; Sultana, C. M.; Lee, C.; Lin, P.; Laskin, J.; Laskin, A.; Dowling, J. A.; Qin, Z.; Cappa, C. D.; Bertram, T. H.; Tivanski, A. V.; Stone, E. A.; Prather, K. A.; Grassian, V. H. Molecular diversity of sea spray aerosol particles: impact of ocean biology on particle composition and hygroscopicity. *Chem.* **2017**, *2*, 655−667.
(20) Craig, R. L.; Bondy, A. L.; Ault, A. P. Surface enhanced Raman spectroscopy enables observations of previously undetectable secondary organic aerosol components at the individual particle level. *Anal. Chem.* **2015**, *87*, 7510−7514.
(21) Kirpes, R. M.; Bondy, A. L.; Bonanno, D.; Moffet, R. C.; Wang, B.; Laskin, A.; Ault, A.; Pratt, K. Secondary sulfate is internally mixed with sea spray aerosol and organic aerosol in the winter Arctic. *Atmos. Chem. Phys.* **2018**, *18*, 3937−3949.
(22) Deng, C.; Brooks, S. D.; Vidaurre, G.; Thornton, D. C. O. Using Raman microspectroscopy to determine chemical composition and mixing state of airborne marine aerosols over the pacific ocean. *Aerosol Sci. Technol.* **2014**, *48*, 193−206.
(23) Yoo, H.; Lee, H.; Park, C.; Shin, D.; Ro, C. U. Novel single-particle analytical technique for submicron atmospheric aerosols:

combined use of dark-field scattering and surface-enhanced Raman spectroscopy. *Anal. Chem.* **2022**, *94*, 13028−13035.
(24) Ault, A.; Zhao, D.; Ebben, C. J.; Tauber, M. J.; Geiger, F. M.; Prather, K. A.; Grassian, V. H. Raman microspectroscopy and vibrational sum frequency generation spectroscopy as probes of the bulk and surface compositions of size-resolved sea spray aerosol particles. *Phys. Chem. Chem. Phys.* **2013**, *15*, 6206−6214.
(25) Trueblood, J. V.; Wang, X.; Or, V. W.; Alves, M. R.; Santander, M. V.; Prather, K. A.; Grassian, V. H. The old and the new: aging of sea spray aerosol and formation of secondary marine aerosol through oh oxidation reactions. *ACS Earth and Space Chemistry* **2019**, *3*, 2307−2314.
(26) Kim, D.; Grassian, V. H. Analysis of micro- and nanoscale heterogeneities within environmentally relevant thin films containing biological components; oxyanions and minerals using AFM-PTIR spectroscopy. *Environmental Science: Processes and Impacts* **2023**, *25*, 484−495.
(27) Starostina, N.; Brodsky, M.; Prikhodko, S.; Hoo, C. M.; Mecartney, M. L.; West, P. AFM capabilities in characterization of particles and surfaces: From angstroms to microns. *J. Cosmet. Sci.* **2009**, *31*, 241.
(28) Lee, H. D.; Morris, H. S.; Laskina, O.; Sultana, C. M.; Lee, C.; Jayarathne, T.; Cox, J. L.; Wang, X.; Hasenecz, E. S.; DeMott, P. J.; et al. Organic enrichment; physical phase state; and surface tension depression of nascent core-shell sea spray aerosols during two phytoplankton blooms. *ACS Earth and Space Chemistry* **2020**, *4*, 650−660.
(29) He, S.; Bouzy, P.; Stone, N.; Ward, C.; Hamerton, I. Analysis of the chemical distribution of self-assembled microdomainswith the selective localization of amine- functionalized graphenenanoplatelets by optical photothermal infrared microspectroscopy. *Anal. Chem.* **2022**, *94*, 11848−11855.
(30) Ahn, T.; Jueckstock, M.; Mandair, G. S.; Henderson, J.; Sinder, B. P.; Kozloff, K. M.; Banaszak Holl, M. M. Matrix/mineral ratio and domain size variation with bone tissue age: A photothermal infrared study. *J. Struct. Biol.* **2022**, *214*, No. 107878.
(31) Mirrielees, J. A.; Kirpes, R. M.; Haas, S. M.; Rauschenberg, C. D.; Matrai, P. A.; Remenapp, A.; Boschi, V. L.; Grannas, A. M.; Pratt, K. A.; Ault, A. P. Probing individual particles generated at the freshwater−seawater interface through combined Raman; photothermal infrared; and x-ray spectroscopic characterization. *ACS Measurements Science Au* **2022**, *2*, 605−619.
(32) Olson, N. E.; Xiao, Y.; Lei, Z.; Ault, A. P. Simultaneous optical photothermal infrared (O-PTIR) and Raman spectroscopy of submicrometer atmospheric particles. *Anal. Chem.* **2020**, *92*, 9932−9939.
(33) Li, X.; Xu, J.; Cheng, J. X. Raman-integrated optical photothermal infrared microscopy: technology and applications. *Molecular and Laser Spectroscopy: Advances and Applications* **2022**, *3*, 281−303.
(34) Kansiz, M.; Prater, C.; Dillon, E.; Lo, M.; Anderson, J.; Marcott, C.; Demissie, A.; Chen, Y.; Kunkel, G. Optical photothermal infrared microspectroscopy with simultaneous Raman−A new non-contact failure analysis technique for identification of < 10 μm organic contamination in the hard drive and other electronics industries. *Microscopy Today* **2020**, *28*, 26−36.
(35) Lavine, B.; Almirall, J.; Muehlethaler, C.; Neumann, C.; Workman, J. Criteria for comparing infrared spectra−A review of the forensic and analytical chemistry literature. *Forensic Chemistry* **2020**, *18*, No. 100224.
(36) Samuel, A. Z.; Mukojima, R.; Horii, S.; Ando, M.; Egashira, S.; Nakashima, T.; Iwatsuki, M.; Takeyama, H. On selecting a suitable spectral matching method for automated analytical applications of Raman spectroscopy. *ACS Omega* **2021**, *6*, 2060−2065.
(37) Penezić, A.; Drozdowska, V.; Novak, T.; Gašparović, B. Distribution and characterization of organic matter within the sea surface microlayer in the Gulf of Gdańsk. *Oceanologia* **2022**, *64*, 631−660.
(38) Burdette, T. C.; Bramblett, R. L.; Zimmermann, K.; Frossard, A. A. "Influence of air mass source regions on signatures of surface-active organic molecules in size resolved atmospheric aerosol particles. *ACS Earth and Space. Chemistry* **2023**, *7*, 1578−1591.
(39) Lewis, S.; Russell, L. M.; Saliba, G.; Quinn, P.; Bates, T.; Carlson, C.; Baetge, N.; Aluwihare, L.; Boss, E.; Frossard, A. A.; Bell, T. G.; Behrenfeld, M. J. Characterization of sea surface microlayer and marine aerosol rganic composition using STXM-NEXAFS microscopy and FTIR Spectroscopy. *ACS Earth Space Chem.* **2022**, *6*, 1899−1913.
(40) Triesch, N.; van Pinxteren, M.; Frka, S.; Stolle, C.; Spranger, T.; Hoffmann, E. H.; Gong, X.; Wex, H.; Schulz-Bull, D.; Gašparovic, B.; Herrmann, H. Concerted measurements of lipids in seawater and on submicrometer aerosol particles at the Cabo Verde islands: biogenic sources; selective transfer and high enrichments. *Atmos. Chem. Phys.* **2021**, *21*, 4267−4283.
(41) Li, S.; Du, L.; Tsona, N. T.; Wang, W. The interaction of trace heavy metal with lipid monolayer in the sea surface microlayer. *Chemosphere* **2018**, *196*, 323−330.
(42) Gašparović, B.; Penezić, A.; Lampitt, R. S.; Sudasinghe, N.; Schaub, T. Free fatty acids; tri-; di- and monoacylglycerol production and depth-related cycling in the Northeast Atlantic. *Marine Chemistry* **2016**, *186*, 101−109.
(43) Mayer, K. J.; Sauer, J. S.; Dinasquet, J.; Prather, K. A. CAICE studies: Insights from a decade of ocean−atmosphere experiments in the laboratory. *Acc. Chem. Res.* **2020**, *53*, 2510−2520.
(44) Laskina, O.; Morris, H. S.; Grandquist, J. R.; Estillore, A. D.; Stone, E. A.; Grassian, V. H.; Tivanski, A. V. Substrate-deposited sea spray aerosol particles: Inter-comparison study of analytical method, substrate and storage conditions on particle size, phase and morphology. *Environ. Sci. Technol.* **2015**, *49*, 13447−13453.
(45) Wang, X.; Sultana, C. M.; Trueblood, J.; Hill, T. C. J.; Malfatti, F.; Lee, C.; Laskina, O.; Moore, K. A.; Beall, C. M.; McCluskey, C. S.; Cornwell, G. C.; Zhou, Y.; Cox, J. L.; Pendergraft, M. A.; Santander, M. V.; Bertram, T. H.; Cappa, C. D.; Azam, F.; DeMott, P. J.; Grassian, V. H.; Prather, K. A. Microbial control of sea spray aerosol composition: A tale of two blooms *ACS Central. Science* **2015**, *1*, 124−131.
(46) Sedgwick, P. Pearson's correlation coefficient. *BMJ.* **2012**, *345*, No. e4483.
(47) Henschel, H.; Andersson, A. T.; Jespers, W.; Mehdi Ghahremanpour, M.; van der Spoel, D. Theoretical infrared spectra: Quantitative similarity measures and force fields". *J. Chem. Theory Comput.* **2020**, *16*, 3307−3315.
(48) Sinclair, R. G.; McKay, A. F.; Jones, R. N. The infrared absorption spectra of saturated fatty acids and esters. *J. Am. Chem. Soc.* **1952**, *74*, 2570−2575.
(49) Corish, P. J.; Chapman, D. The infrared spectra of some monocarboxylic acids. *Journal of the Chemical Society* **1957**, 1746−1751.
(50) Czamara, K.; Majzner, K.; Pacia, M. Z.; Kochan, K.; Kaczor, A.; Baranska, M. Raman spectroscopy of lipids: A review. *J. Raman Spectrosc.* **2015**, *46*, 4−20.
(51) Wiercigroch, E.; Szafraniec, E.; Czamara, K.; Pacia, M. Z.; Majzner, K.; Kochan, K.; Kaczor, A.; Baranska, M.; Malek, K. Raman and infrared spectroscopy of carbohydrates: A review. *Spectrochimica Acta Part A: Molecular and Biomolecular Spectroscopy* **2017**, *185*, 317−335.
(52) Banas, A. M.; Banas, K.; Chu, T. T. T.; Naidu, R.; Hutchinson, P. E.; Agrawal, R.; Lo, M. K. F.; Kansiz, M.; Roy, A.; Chandramohanadas, R.; Breese, M. B. H. Comparing infrared spectroscopic methods for the characterization of Plasmodium falciparum-infected human erythrocytes. *Commun. Chem.* **2021**, *4*, 129.
(53) Jamieson, L. E.; Li, A.; Faulds, K.; Graham, D. Ratiometric analysis using Raman spectroscopy as a powerful predictor of structural properties of fatty acids. *Royal Society Open Science* **2018**, *5*, No. 181483.

https://doi.org/10.1021/acsmeasuresciau.4c00033
ACS Meas. Sci. Au XXXX, XXX, XXX−XXX

(54) Filopoulou, A.; Vlachou, S.; Boyatzis, S. C. Fatty acids and their metal salts: a review of their infrared spectra in light of their presence in cultural heritage. *Molecules* **2021**, *26*, 6005.
(55) Meiklejohn, R. A.; Meyer, R. J.; Aronovic, S. M.; Schuette, H. A.; Meloche, V. W. Characterization of long-chain fatty acids by infrared spectroscopy. *Anal. Chem.* **1957**, *29*, 329−334.
(56) Ramer, G.; Aksyuk, V. A.; Centrone, A. Quantitative Chemical Analysis at the Nanoscale Using the Photothermal Induced Resonance Technique. *Anal. Chem.* **2017**, *89*, 13524−13531.
(57) Schwartz, J. J.; Jakob, D. S.; Centrone, A. A guide to nanoscale IR spectroscopy: resonance enhanced transduction in contact and tapping mode AFM-IR. *Chem. Soc. Rev.* **2022**, *51*, 5248−5267.
(58) Hinrichs, K.; Shaykhutdinov, T. Polarization-dependent atomic force microscopy−infrared spectroscopy (AFM-IR): Infrared nano-polarimetric analysis of structure and anisotropy of thin films and surfaces. *Appl. Spectrosc.* **2018**, *72*, 817−832.
(59) Kurouski, D.; Dazzi, A.; Zenobi, R.; Centrone, A. Infrared and Raman chemical imaging and spectroscopy at the nanoscale. *Chem. Soc. Rev.* **2020**, *49*, 3315−3347.
(60) Madawala, C. K.; Molina, C.; Kim, D.; Gamage, D. K.; Sun, M.; Leibensperger, R. J.; Mehndiratta, L.; Lee, J.; Kaluarachchi, C. P.; Kimble, K.'L. A.; Sandstrom, G.; Harb, C.; Dinasquet, J.; Malfatti, F.; Prather, K. A.; Deane, G. B.; Stokes, M. D.; Lee, C.; Slade, J. H.; Stone, E. A.; Grassian, V. H.; Tivanski, A. V. Effects of Wind Speed on Size-Dependent Morphology and Composition of Sea Spray Aerosols. *ACS Earth Space Chem.* **2024**, *8*, 1609−1622.
(61) Tumminello, P. R.; Niles, R.; Valdez, V.; Madawala, C. K.; Gamage, D. K.; Kimble, K. A.; Leibensperger, R. J.; Huang, C.; Kaluarachchi, C.; Dinasquet, J.; Malfatti, F.; Lee, C.; Deane, G. B.; Stokes, M. D.; Stone, E.; Tivanski, A.; Prather, K. A.; Boor, B. E.; Slade, J. H. Size-Dependent Nascent Sea Spray Aerosol Bounce Fractions and Estimated Viscosity: The Role of Divalent Cation Enrichment, Surface Tension, and the Kelvin Effect. *Environ. Sci. Technol.* **2024**, *58*, 19666−19678.
(62) Machado, W.; Franchini, J. C.; de Fatima Guimaraes, M.; Filho, J. T. Spectroscopic characterization of humic and fulvic acids in soil aggregates, Brazil. *Heliyon* **2020**, *6*, No. e04078.
(63) Prieto-Taboada, N.; Gómez-Laserna, O.; Martínez-Arkarazo, I.; Olazabal, M.Á; Madariaga, J. M. Raman spectra of the different phases in the $CaSO_4$−H_2O system. *Anal. Chem.* **2014**, *86*, 10131−10137.
(64) Ault, A. P.; Guasco, T. L.; Baltrusaitis, J.; Ryder, O. S.; Trueblood, J. V.; Collins, D. B.; Ruppel, M. J.; Cuadra-Rodriguez, L. A.; Prather, K. A.; Grassian, V. H. Nitric acid reacted wave-flume generated sea spray aerosol particles: Diverse reactivities between and within individual particles. *J. Phys. Chem. Lett.* **2014**, *5*, 2493−2500.
(65) Alhazmi, H. A. FT-IR spectroscopy for the identification of binding sites and measurements of the binding interactions of important metal ions with bovine serum albumin. *Scientia Pharmaceutica* **2019**, *87*, 5.
(66) Prather, K. A.; Bertram, T. H.; Grassian, V. H.; Deane, G. B.; Stokes, M. D.; DeMott, P. J.; Aluwihare, L. I.; Palenik, B. P.; Azam, F.; Seinfeld, J. H.; et al. Bringing the ocean into the laboratory to probe the chemical complexity of sea spray aerosol. *Proc. Natl. Acad. Sci. U. S. A.* **2013**, *110*, 7550−7555.
(67) Sultana, C. M.; Collins, D. B.; Prather, K. A. Effect of Structural Heterogeneity in Chemical Composition on Online Single-Particle Mass Spectrometry Analysis of Sea Spray Aerosol Particles. *Environ. Sci. Technol.* **2017**, *51*, 3660−3668.
(68) Kaluarachchi, C. P.; Or, V. W.; Lan, Y.; Madawala, C. K.; Hasenecz, E. S.; Crocker, D. R.; Morris, C. K.; Lee, H. D.; Mayer, K. J.; Sauer, J. S.; et al. Size-dependent morphology; composition; phase state; and water uptake of nascent submicrometer sea spray aerosols during a phytoplankton bloom. *ACS Earth and Space Chemistry* **2022**, *6*, 116−130.
(69) DeMott, P. J.; Hill, T. C. J.; McCluskey, C. S.; Prather, K. A.; Collins, D. B.; Sullivan, R. C.; Ruppel, M. J.; Mason, R. H.; Irish, V. E.; Lee, T.; Hwang, C. Y.; Rhee, T. S.; Snider, J. R.; McMeeking, G. R.; Dhaniyala, S.; Lewis, E. R.; Wentzell, J. J. B.; Abbatt, J.; Lee, C.; Sultana, C. M.; Ault, A. P.; Axson, J. L.; Diaz Martinez, M.; Venero, I.; Santos-Figueroa, G.; Stokes, M. D.; Deane, G. B.; Mayol-Bracero, O. L.; Grassian, V. H.; Bertram, T. H.; Bertram, A. K.; Moffett, B. F.; Franc, G. D. Sea Spray Aerosol as a Unique Source of Ice Nucleating Particles. *Proc. Natl. Acad. Sci. U. S. A.* **2016**, *113*, 5797−5803.
(70) Mehndiratta, L.; Lyp, A. E.; Slade, J. H.; Grassian, V. H. Immersion Ice Nucleation of Atmospherically Relevant Lipid Particles. *Environ. Sci.: Atmos.* **2024**, *4*, 1239.

https://doi.org/10.1021/acsmeasuresciau.4c00033
ACS Meas. Sci. Au XXXX, XXX, XXX−XXX